Graphene reduction dynamics unveiled

2015 2D Mater. 2 031003

(http://iopscience.iop.org/2053-1583/2/3/031003)

2D Materials

RECEIVED
24 April 2015

REVISED
11 June 2015

ACCEPTED FOR PUBLICATION
8 July 2015

PUBLISHED
6 August 2015

LETTER

Graphene reduction dynamics unveiled

Hung-Chieh Tsai[1], **Hung-Wei Shiu**[2], **Min-Chiang Chuang**[1], **Chia-Hao Chen**[2], **Ching-Yuan Su**[3], **Jonathon David White**[4] **and Wei Yen Woon**[1]

[1] Department of Physics, National Central University, Jungli, 32054, Taiwan
[2] National Synchrotron Radiation Research Center (NSRRC), Hsinchu 30076, Taiwan
[3] Graduate Institute of Energy Engineering, National Central University, Jungli, 32054, Taiwan
[4] Dept. of Photonics Engineering, Yuan Ze University, Taoyuan 32003, Taiwan

E-mail: wywoon@phy.ncu.edu.tw

Keywords: graphene, defects, scanning probe lithography, reduction, photoelectron spectroscopy

Abstract

The reduction dynamics of micron-sized defects created on chemical vapor deposition- (CVD) grown graphene through scanning probe lithography (SPL) is reported here. CVD-grown graphene was locally oxidized using SPL and subsequently reduced, making use of a focused beam of soft x-rays. During this whole process, the reduction dynamics was monitored using a combination of micro-Raman spectroscopy (μ-RS) and micro-x-ray photoelectron spectroscopy (μ-XPS). After x-ray reduction, the graphene film was found to be chemically identical (μ-XPS) but structurally different (μ-RS) from the original graphene. During reduction the population of C–C bonds was found to first increase dramatically and then decrease exponentially. By modeling the dynamics of the C=O → C–O → C–C → C=C reduction process with four coupled-rate equations and three rate constants, the conversion from C–C to C=C bonds was found to be the limiting rate.

1. Introduction

Since their emergence in 2004, two-dimensional (2D) materials have drawn vast research activities and ignited high expectation for their potential in various applications [1]. Within this plethora of 2D materials, high mobility and a high surface-to-volume ratio have made graphene, in particular, one of the most highly anticipated candidates to replace current bulk materials in electronic and energy storage applications [2, 3].

As the lack of a bandgap in intrinsic graphene limits its applicability [4], considerable effort has been made to create bandgaps in graphene through various methods, including modification of sp^3/sp^2 hybridization by functionalization, external bias, defect engineering, and topological confinement effects [5–8]. An alternative path for bandgap engineering in graphene-related materials is through controlled reduction of graphene oxide (GO) [9]. Solvent-based techniques have been demonstrated to be effective for GO reduction [10], as evidenced by the dramatic reduction in photoluminescence and increase in electric conductivity observed as GO is reduced [11]. While it is well known that the GO reduction involves the breaking and reconstruction of C–O– and C–C–related bonds [12], nevertheless, the exact pathways and dynamics for reduction have not been thoroughly elucidated experimentally.

In addition to bandgap engineering, *controlled* defect introduction into (or doping of) the originally perfect 2D honeycomb lattice may open up more dimensions for tuning of *local* graphene properties such as surface reactivity [13]. Conversely, graphene grown by any method other than mechanical exfoliation contains defects [14]. For example, chemical vapor deposition- (CVD) grown graphene acquires *uncontrolled* defects through generation of grain boundaries, vacancies, and impurities incorporated during the nucleation and growth period and the subsequent transferring processes [15, 16]. Understanding the *local* dynamics of both defect generation and reduction is necessary to enable graphene-related materials to be modified in a controllable and systematic way.

In our previous work, we have demonstrated the feasibility of applying scanning probe lithography (SPL), a mask-less technique that enables nanometer-scale patterning on metallic or semiconducting

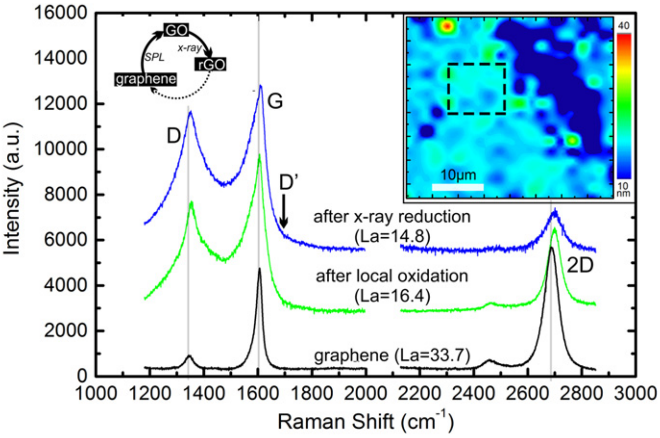

Figure 1. Micro-Raman spectra before defect generation (black line); after defect generation using SPL but before x-ray reduction (green line); and after x-ray reduction (blue line). Spectra are offset for clarity. Inset: Mapping of the average distance between defects (L_D) for the graphene film before the generation of defects by SPL. L_D is obtained from the intensity ratio of the D and G peaks using equation (1) (see text). The spatial resolution of the right inset is 1 μm. A black box indicates the area in which localized defective regions were produced. Left inset: Summary of the processing steps used in this paper.

substrates [17], to generate local strain in a graphene sheet by the formation of subsurface silicon oxide protrusion through a thin buffer oxide [18]. By adjusting the SPL parameters, local anodic oxidation or vacancy formation through ion bombardment has been demonstrated [19]. Byun *et al* have shown that it is possible to reduce these locally oxidized graphene areas by heat treatments [20]. Nevertheless, the reduction dynamics of those locally oxidized regions in CVD-grown graphene has not been studied in detail. This is the goal of this paper. We first locally oxidize graphene via SPL and then reduce these defective areas, making use of low-energy x-rays (figure 1 (left inset)). Throughout the reduction process, micro-Raman spectroscopy (μ-RS) and micro-photoelectron spectroscopy (μ-XPS) were employed to monitor the changing structural and chemical composition during reduction. The reduction dynamics can be described with a set of coupled differential equations with three unambiguously identified characteristic time scales, which correlate to the dissociation/creation of respective carbon-oxygen-related bonds during the reduction process.

2. Experimental techniques

Monolayer graphene was grown on 25 μm-thick copper foil in a quartz tube furnace system using CVD [24, 25]. Under vacuum conditions of 10 mTorr and at a temperature of 1000 °C, H_2 was first introduced (flow rate = 2 sccm) for 40 min, followed by methane (35 sccm) for 15 min Quick cooling was then applied (300 °C min^{-1}) under continuous methane and hydrogen gas flows. A layer of polymethylmethacrylate (PMMA) was then spin-coated onto the as-grown films, and iron (III) nitrate was used to etch away the copper foil. Finally, films were transferred to 100 nm-thick, oxide-buffered SiO_2/Si wafers, and the PMMA was dissolved with acetone. All measurements were done on the SiO_2/Si substrate.

The transferred graphene films were locally modified using SPL, making use of a modified contact-mode atomic force microscope (AFM, Bruker Innova) with a conventional conductive AFM probe (Pt/Ir coated point-probe series, Nanosensor). Using this tip at a bias voltage of −10 V, a 5 × 5 grid of 1.5 × 1.5 μm^2 squares was oxidized by SPL, making use of the built-in software (Nanoplot, Bruker). As the process is sensitive to humidity, a sealed container was used to maintain the relative humidity at ~55% throughout the SPL process [18, 19].

Selected defective areas were then reduced under ultra-high vacuum (10^{-9} Torr), using focused soft x-rays (photon energy hν = 380 eV, beam diameter ϕ = 100 nm) generated on the beam line (SPEM end station, 09A1) of the National Synchrotron Radiation Research Center (NSRRC, Hsinchu, Taiwan) [26].

The samples were monitored throughout processing using μ-RS and μ-XPS (exposure time = 0.02 s using the same beam line as used for reduction), along with atomic force microscopy and lateral force microscopy (LFM). μ-RS was used to first spatially characterize the graphene film (I_{2D}/I_G; symmetry of the 2D band; defect density) [27, 28]. These μ-RS images were acquired using a confocal micro-Raman spectrometer (Lab Ram HR, Horiba) employing a λ = 532 nm DPSS laser for excitation focused onto the sample plane by a 100X, NA = 0.9 objective lens. A motorized stage (step size = 0.5 μm) was employed to achieve a spatial resolution of ~1 μm. After patterning, topographical and lateral force information were acquired using the same tip that was used for SPL. For more refined structural detail, a tapping-mode AFM with a sharp probe (SSS series, Nanosensor) was employed to avoid image distortion.

3. Results and discussion

As-grown graphene films were first imaged using μ-RS in order to identify a suitable area for SPL modification. In particular, the intensities of the G ($\sim$1580 cm^{-1}), 2D ($\sim$2680 cm^{-1}), and forbidden D ($\sim$1350 cm^{-1}) were observed to assess the quality of the film (figure 1 (black line)). The effective crystalline size (L_a) was then estimated, using the empirically derived relationship [21]:

$$L_a\,[nm] = \sqrt{(1.8 \pm 0.5) \times 10^{-9} \lambda_{laser}^{4} \left(\frac{I_D}{I_G}\right)^{-1}} \quad (1)$$

where I_D is the intensity of the forbidden D band, I_G is the intensity of the G band, and λ_{laser} is the wavelength of excitation light in nm (532 nm in our case). (Note that this formula is only valid in the low-defect density regime, i.e., for $L_a > 10$ nm.) figure 1 (inset) presents the mapping of L_a for the graphene film based on this formula. As seen in this figure, the defect density varies from $L_a > 50$ nm to $L_a < 10$ nm in this region of the film. For SPL processing, we chose a region (figure 1 (inset), black box) where the defect density was at an intermediate level. Figure 1 (black line) presents a typical μ-RS spectra for this region. As can be seen in the figure, $I_D/I_G \sim 0.13$ ($L_a \sim 33.66$ nm), and (I_{2D}/I_G) ~ 1.30.

Within this region, SPL was employed to modify a 5×5 array of $1.5 \times 1.5\ \mu\text{m}^2$ squares. Figure 2 presents the optical, LFM, and μ-XPS images of the film after sample modification. Modification of the graphene film is clearly visible in all three imaging modalities. As can be seen in these images, modification was successful in 24 of 25 of the locations in which it was attempted. The strong contrast in the LFM images indicates that friction has been increased in treated regions; i.e., the physical properties of graphene have been modified by the SPL process. Topographical images (not shown) indicate that this LFM contrast results from depressions with a depth of <1 nm [19]. The image (figure 2(c) (bottom left)) of the C1S μ-XPS spectra (taken at 284.4 eV) reflects the C=C bond strength. The bright (dark) spots represent pristine-like (defected) graphene, indicating a substantial reduction in the number of C=C bonds in the SPL-processed regions [22]. Returning to figure 1, the green line presents a typical μ-RS spectrum taken in the SPL-processed area. A significant increase in D band intensity, and a corresponding decrease in the intensity of the G and 2D bands relative to the pristine, has been induced by SPL. For this region, the effective crystalline size L_a, as measured through I_D/I_G, has decreased down to 16 nm. Overall, for all locally modified regions, L_a decreases significantly down to <20 nm, indicating the creation of defects through the SPL process.

After recording the C1S μ-XPS spectra map, the soft x-ray beam was successively focused on six of the locally oxidized regions. Complete μ-XPS spectra (exposure time = 20 s) were taken at 20 s intervals. Figure 2(d) (bottom right) maps the C1S μ-XPS spectra after 400 s of irradiation. As can be seen in comparing the images before and after irradiation, the intensity at 284.4 eV in each of the six irradiated areas has recovered to the level of the pristine film, indicating an almost complete recovery of C=C bonds. We believe this is the result of low-energy electrons generated by the absorption of x-ray radiation. These low-energy photoelectrons lead to a mild bombardment in the illuminated area and thus local heating of the defected region, i.e., a process similar to ion/electron irradiation annealing [23].

This bond destruction and reconstruction is seen more clearly in figure 3, which compares the μ-XPS spectra of the CVD-grown graphene with the spectra after oxidation and that taken after reduction. Prior to SPL treatment, the XPS spectrum taken at a typical graphene site (La = 33.7 nm) is composed of a sharp C=C peak, a small C–C peak, and a very small C–O peak. These peaks are typical for CVD-grown graphene, in which natural defects exist. After SPL, the C=C peak intensity drastically decreases, while the C–O and C=O peaks grow significantly. Following x-ray irradiation, the C=C peak intensity recovers almost fully back to the original peak height after XPS irradiation, while the C–O and C=O peaks nearly disappear. Throughout the process the C–C peak intensity remains approximately constant, increasingly only slightly during the oxidation process and returning to its original level after oxidation. However, we do note that the fitted peak width of the C=C peak has increased slightly during processing.

While it would be tempting to conclude from the chemical data that the graphene film has been restored to its pristine state (i.e., to that prior to SPL treatment), other imaging modalities indicate otherwise. While there was near-complete recovery of the C=C bond intensity, this recovery was not reflected in either the optical or LFM images (see figure S2 in the supplementary materials). We thus turn to μ-RS to understand the structure of the reduced film. As shown in the blue curve in figure 1, I_G/I_D (and hence L_a) remains relatively invariant with x-ray irradiation, suggesting that there has been little change in the average distance between defects (L_a). There is no recovery of domain size to that of the defect-free pristine-like film. In addition, there is also a significant drop in the peak intensity of the 2D band. Similar observations have been reported in studies of GO reduction. In the case of GO reduction, significant drops in I_G/I_D and I_{2D} were found and explained in terms of the formation of small graphene flakes and graphitization through out-of-plane bonding [22]. Our observation indicates there is no structural recovery during x-ray irradiation, despite the reduction of the C=O and C–O bonds. It is probable that the newly created C=C bonds form a complex structure that is highly stable and 'augmented' into the pristine graphene crystal surroundings. However, contrary to GO, which is

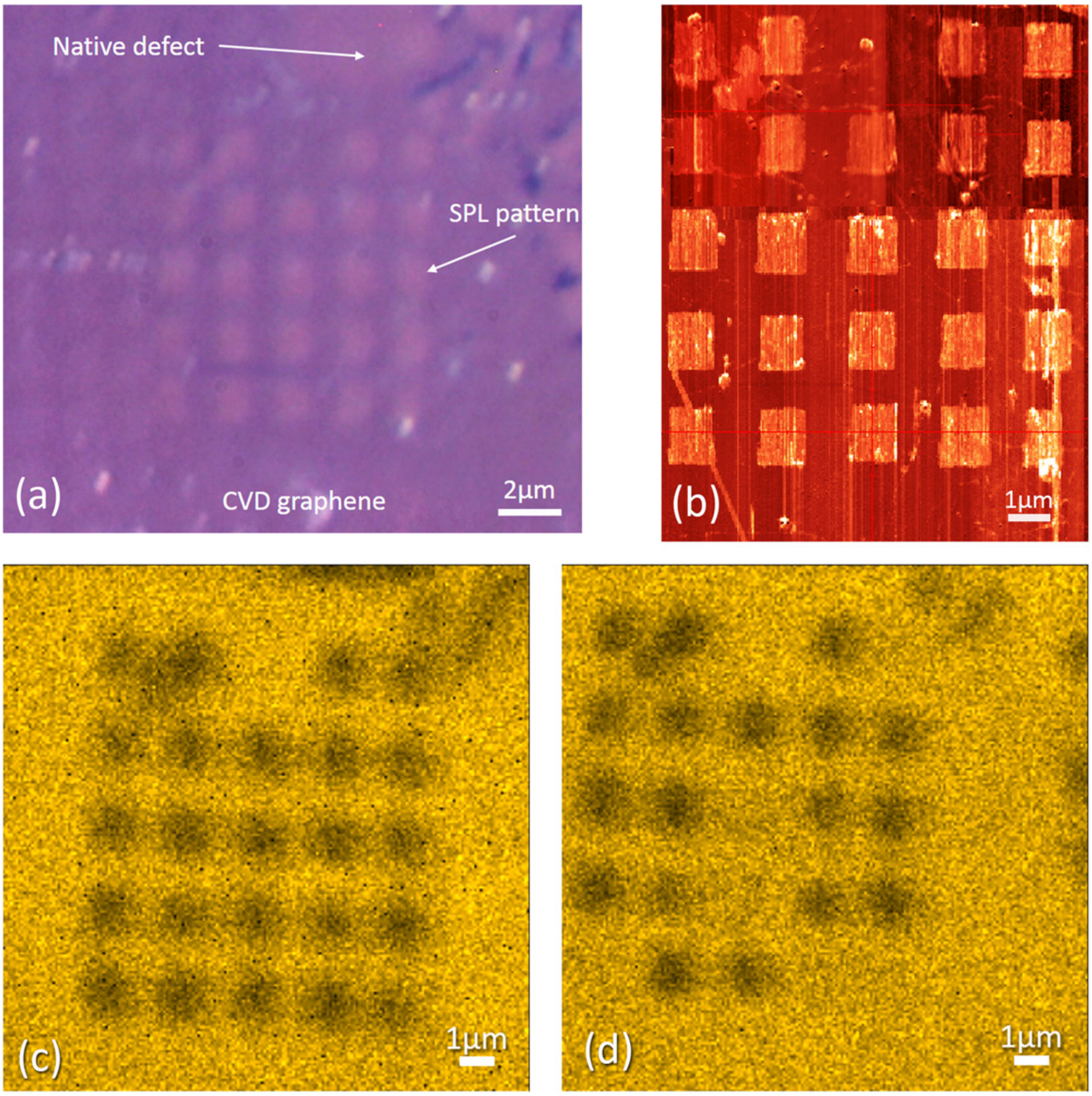

Figure 2. Images of SPL-treated graphene. Optical (a) and LFM (b) images taken after SPL treatment but before localized reduction. C1S μ-XPS spectra at 284.4 eV (reflecting the C=C bond strength) taken before (c) and after (d) reduction using soft x-rays. (Exposure time = 0.02 s).

uniformly defective everywhere, in our case there is a vast pristine graphene crystal around the micron-sized defects created through SPL that could act as the crystalline seed for the regrowth of graphene flakes under thermal annealing. The insignificant change in L_a is then considered as a combined result of (1) breaking of oxygen-related bonds, (2) creation of C–C bonds, and (3) augmentation into the existing sp^2 C=C honeycomb network.

We now move to the main part of our study: the dynamics of the reduction process. The typical evolution of C1S spectra is shown in figure 4, starting from the spectra for the locally oxidized sample. This waterfall spectra clearly shows that the C=O and C–O peaks diminish, while the C–C and C=C peaks grow simultaneously. Typically only a stable single C=C peak can be found after 80–100 s of illumination, as the peaks corresponding to the C=O, C–O, and C–C bonds have all diminished. This evolution is seen more clearly in figure 5, where the evolution of the bond concentration (obtained from the area under the peaks) is plotted as a function of time. (Six sets of XPS data taken from different locations in the graphene sheet were added.) The decay of the C=O peak with time appears to be simply a single exponential decay. Considering the C=C peak, there appears to be a slight delay in the start of growth, followed by a period of approximately exponential growth, and then, as saturation begins, the growth slows down, and after a period of time, constant intensity. This suggests that (1) the dynamics for the C=C peak can be fit by a multiple exponent growth function, and (2) the C=O bonds are not directly converted to C=C bonds but involve intermediate species. The peak evolution of the remaining two peaks is more complicated and is clearly multi-exponential, with both a growth and decay phase. In light of this and the bonds involved it seems logical to model the bond formation and dissolution as a set of sequential steps, i.e.,

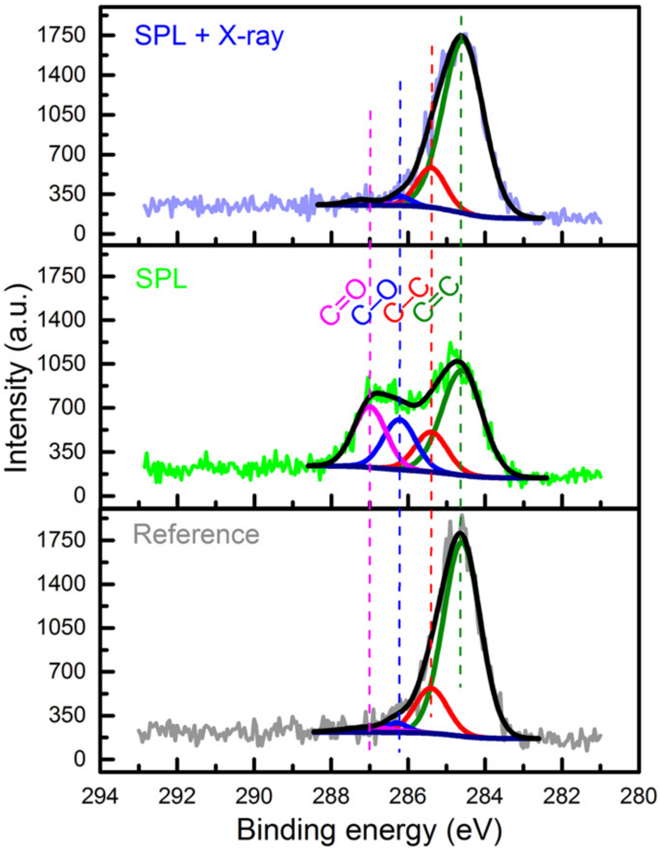

Figure 3. Micro-x-ray photoelectron spectra (μ-XPS) taken before defect generation (bottom, gray line); after defect generation using SPL but before x-ray reduction (middle, green line); and after x-ray reduction (top, blue line). Fitted peaks that represent C=O (288 eV) (magenta), C–O (286 eV) (blue), C–C (285.5 eV) (red), and C=C (284.4 eV) (green), and their superposition (black) are presented along with the raw data.

C=O → C–O → C–C → C=C, where the process stops. Thus we propose that the dynamics be modeled by a set of four linearly coupled equations with three rate constants:

$$\frac{\mathrm{d}N_{C=O}}{\mathrm{d}t} = -k_{C=0\rightarrow C-O}\left(N_{C=O} - N'_{C=O}\right) \tag{1a}$$

$$\frac{\mathrm{d}N_{C-O}}{\mathrm{d}t} = +k_{C=0\rightarrow C-O}\left(N_{C=O} - N'_{C=O}\right) - k_{C-0\rightarrow C-C}\left(N_{C-O} - N'_{C-O}\right) \tag{1b}$$

$$\frac{\mathrm{d}N_{C-C}}{\mathrm{d}t} = +k_{C-0\rightarrow C-C}\left(N_{C-O} - N'_{C-O}\right) - k_{C-C\rightarrow C=C}\left(N_{C-C} - N'_{C-C}\right) \tag{1c}$$

$$\frac{\mathrm{d}N_{C-O}}{\mathrm{d}t} = +k_{C-C\rightarrow C=C}\left(N_{C=C} - N'_{C=C}\right) \tag{1d}$$

where the Ns represent the respective bond densities (implicitly a function of time), $\boldsymbol{k}$ represents the corresponding rate constants for the bond dissociation/creation, and N' are constants related to their corresponding steady-state bond concentrations at the end of the reduction process. Under the assumption that the reduction process is driven by localized heating, the rate constants are expected to have a similar dependence on soft x-ray irradiance, and, thus, instead of the respective rate constant, it is more reasonable to present the reduced rate constants using the definitions:

$$\begin{aligned} k\left(E_e, L_a\right) &= k_{C=0\rightarrow C-O} \\ \kappa_1 &= k_{C-0\rightarrow C-C}/k_{C=0\rightarrow C-O} \\ \kappa_2 &= k_{C-C\rightarrow C=C}/k_{C=0\rightarrow C-O} \end{aligned} \tag{2}$$

where we have explicitly shown only k is a function of x-ray irradiance (E_e) and physical details of the defect structure (L_a).

Least-squares fitting of the above equations to the data leads to $k = 0.055$ (s^{-1}) for $L_a \sim 15$ nm, $\kappa_1 = 1.09$, and $\kappa_2 = 0.73$. The theoretical fit is shown as lines in figure 5. Good agreement is achieved between the experimental data and theoretical curve fit, suggesting that the dynamics of the reduction are well modeled by the above equations. These results indicate that the reduction of GO (1) starts from the removal of oxygen-related bonding and ends at the formation of C=C bonds, and (2) occurs in a step-like fashion, with C–O and C–C acting as intermediate species. The bond creation/dissociation rate is higher for the bond (C–O → C–C) that involves only a single covalent bond than that which involves the breaking of the double covalent bond (C=O → C–O). Finally, the conversion of the single- to double-carbon bonds (C–C → C=C) is about 37.5–50% slower than either the reduction of

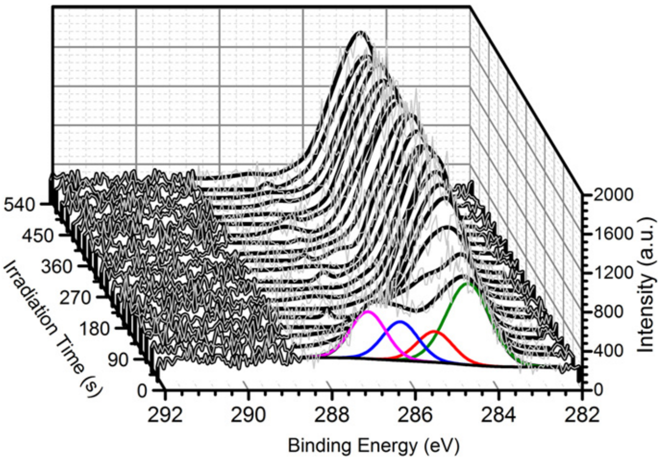

Figure 4. Waterfall diagram illustrating the gradual changes in μ-XPS as a localized defective region is gradually reduced by soft x-rays. Success curves are taken 20 s apart over a period of 400 s.

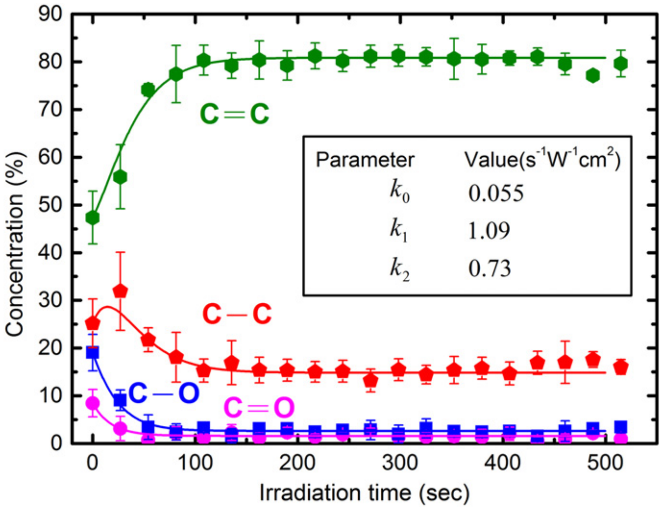

Figure 5. Time evolution of the area under the C–C, C=O, C–O, and C=C μ-XPS peaks. Experimental data are shown as points. The lines represent a best fit using the rate-equations model presented in the text. Inset: Parameters for best fit (see text for details).

the oxygen double bond (i.e., C=O → C–O) or the replacement of the single- carbon oxygen bond with a single carbon-carbon bond, indicating that the conversion from single- to double-carbon bonds is the limiting step. Finally we note that involvement of C–C bond formation and breakage is this process is not evident if one only considers the initial and final states, as shown in figure 3.

We can consider the process as follows: As the C=O and C–O bonds were kinetically formed during the SPL process through the intense ion bombardment of OH^- decomposed from ambient water molecules, as a result, the chemical bond configurations are therefore not expected to be highly thermally stable. Furthermore, since local thermal heating through photoelectron current is not a selective excitation process, it is expected that the bonds with a lower dissociation energy barrier should dissociate first, as observed for the case of C=O and C–O bonds. The bond strength of a double-covalent bond is much stronger than its single-covalent bond counterparts. Based on the above reasoning, it is therefore expected that the dissociation rate of C=O will be lower than C–O bonds, as observed in this experiment. The rate for the conversion of C–C to C=C bonds is much lower than for the reduction of C=O to C–O. It is also noticeable that as the C=C bond density (XPS peak area) became saturated, no further changes can be induced by the x-ray irradiation, indicating that a stable structure was formed in the graphene sheet. The above observation indicates that stable C=C bonds had been formed through the reduction process (not the perfect 2D honeycomb lattice as measured from μ-RS). From the literature, GO reduction through thermal annealing or chemical treatment can efficiently remove functional groups (carbonyl, epoxy, hydroxyl) in GO but is not able to recover the structural defects [22]. From our μ-XPS result, it is conclusive that the x-ray irradiation is able to reduce the oxidized graphene through dissociating C=O and C–O bonds, while the μ-RS indicates incomplete structural recovery, similar to previous findings.

It is also probable that the regrowth dynamics is dependent on initial crystallinity. For example, we have observed much slower reduction dynamics (i.e., reduced value of k) in similar SPL defect structures at locations with low initial L_a, hinting that the characteristic rate for each bond dissociation/creation process depends strongly on the initial crystallinity. In order to understand the dependence of the characteristic time of bond dissociation/creation on initial crystallinity, we have commenced a detailed study on the dependence of reduction dynamics on initial structural conditions.

4. Conclusions

In conclusion, the reduction dynamics of micron-sized defects created on CVD-grown graphene through SPL has been investigated. μ-RS throughout the oxidation reduction process revealed the structural evolution from CVD-grown graphene to oxidized graphene to reduced graphene oxide with a different structure than that of the initial graphene. By *in-situ* measuring the chemical profile of the soft x-ray-irradiated, SPL-induced defects, the evolution of each associated carbon-oxygen bond strength is resolved by μ-XPS. The characteristic rate for each bond dissociation/creation process involved during reduction was modeled using a set of linearly coupled dynamics equation and found to involve sequentially C=O → C–O → C–C → C=C, with the conversion from C–C → C=C determined to be the rate-limiting step. In future work, we are hoping to investigate the reasons for our failure to reduce preexisting C–C bonds leftover from the CVD growth process. A side implication of this work is that while GO can be reduced, care must be taken to ensure that the resulting product is graphene and not just reduced graphene oxide. For this, μ-RS is crucial, as both photoluminescence spectroscopy and μ-XPS provide only information on the chemical nature of the reduced product.

Acknowledgments

This work is supported by the National Science Council of the Republic of China under contract MOST103-2112-M008-019-MY3. We gratefully acknowledge the facility support from NCU CNST.

References

[1] Mas-Balleste R, Gomez-Navarro C, Gomez-Herrero J and Zamora F 2011 2D materials: to graphene and beyond *Nanoscale* **3** 20–30

[2] Novoselov K S, Geim A K, Morozov S V, Jiang D, Zhang Y, Dubonos S V, Grigorieva I V and Firsov A A 2004 Electric field effect in atomically thin carbon films *Science* **306** 666–9

[3] Brownson D A C, Kampouris D K and Banks C E 2011 An overview of graphene in energy production and storage applications *J. Power Sources* **196** 4873–85

[4] Geim A K and Novoselov K S 2007 The rise of graphene *Nat. Mater.* **6** 183–91

[5] Balog R *et al* 2010 Bandgap opening in graphene induced by patterned hydrogen adsorption *Nat. Mater.* **9** 315–9

[6] Zhang Y, Tang T T, Girit C, Hao Z, Martin M C, Zettl A, Crommie M F, Shen Y R and Wang F 2009 Direct observation of a widely tunable bandgap in bilayer graphene *Nature* **459** 820–3

[7] Denis P A and Iribarne F 2013 Comparative study of defect reactivity in graphene *J. Phys. Chem.* C **117** 19048–55

[8] Han M, Özyilmaz B, Zhang Y and Kim P 2007 Energy bandgap engineering of graphene nanoribbons *Phys. Rev. Lett.* **98** 206805

[9] Jung I, Dikin D A, Piner R D and Ruoff R S 2008 Tunable electrical conductivity of individual graphene oxide sheets reduced at 'low' temperatures *Nano Lett.* **8** 4283–7

[10] Zhao J, Pei S, Ren W, Gao L and Cheng H-M 2010 Efficient preparation of large-area graphene oxide sheets for transparent conductive films *ACS Nano* **4** 5245–52

[11] Eda G and Chhowalla M 2010 Chemically derived graphene oxide: towards large-area thin-film electronics and optoelectronics *Adv. Mater.* **22** 2392–415

[12] Stankovich S, Dikin D A, Piner R D, Kohlhaas K A, Kleinhammes A, Jia Y, Wu Y, Nguyen S T and Ruoff R S 2007 Synthesis of graphene-based nanosheets via chemical reduction of exfoliated graphite oxide *Carbon* **45** 1558–65

[13] Robinson J T, Perkins F K, Snow E S, Wei Z and Sheehan P E 2008 Reduced graphene oxide molecular sensors *Nano Lett.* **8** 3137–40

[14] Allen M J, Tung V C and Kaner R B 2009 Honeycomb carbon: a review of graphene *Chem. Rev.* **110** 132–45

[15] Girit Ç Ö *et al* 2009 Graphene at the edge: Stability and dynamics *Science* **323** 1705–8

[16] Gao L, Ni G-X, Liu Y, Liu B, Castro Neto A H and Loh K P 2014 Face-to-face transfer of wafer-scale graphene films *Nature* **505** 190–4

[17] Tseng A A, Notargiacomo A and Chen T P 2005 Nanofabrication by scanning probe microscope lithography: a review *J. Vac. Sci. Technol.* B **23** 877–94

[18] Chuang M-C, Chien H-M, Chain Y-H, Chi G-C, Lee S-W and Woon W Y 2013 Local anodic oxidation kinetics of chemical vapor deposition graphene supported on a thin oxide buffered silicon template *Carbon* **54** 336–42

[19] Chien H-M, Chuang M-C, Tsai H-C, Shiu H-W, Chang L-Y, Chen C-H, Lee S-W, White J D and Woon W-Y 2014 On the nature of defects created on graphene by scanning probe lithography under ambient conditions *Carbon* **80** 318–24

[20] Byun I-S 2011 Nanoscale lithography on monolayer graphene using hydrogenation and oxidation *ACS Nano* **5** 6417–24

[21] Cançado L G, Takai K, Enoki T, Endo M, Kim Y A, Mizusaki H, Jorio A, Coelho L N, Magalhães-Paniago R and Pimenta M A 2006 General equation for the determination of the crystallite size La of nanographite by Raman spectroscopy *Appl. Phys. Lett.* **88** 163106

[22] Yang D 2009 Chemical analysis of graphene oxide films after heat and chemical treatments by x-ray photoelectron and Micro-Raman spectroscopy *Carbon* **47** 145–52

[23] Withers F, Bointon T H, Dubois M, Russo S and Craciun M F 2011 Nanopatterning of fluorinated graphene by electron beam irradiation *Nano Lett.* **11** 3912–6

[24] Li X 2009 Large-area synthesis of high-quality and uniform graphene films on copper foils *Science* **324** 1312–4

[25] Mattevi C, Kim H and Chhowalla M 2011 A review of chemical vapour deposition of graphene on copper *J. Mater. Chem.* **21** 3324–34

[26] Chen C H, Aballe L, Klauser R, Kampen T U and Horn K 2005 Valence band discontinuity at the GaN/SiC(0 0 0 1) heterojunction studied *in situ* by synchrotron-radiation photoelectron spectroscopy *J. Electron Spectrosc. Relat. Phenom.* **144–7** 425–8

[27] Casiraghi C, Pisana S, Novoselov K S, Geim A K and Ferrari A C 2007 Raman fingerprint of charged impurities in graphene *Appl. Phys. Lett.* **91** 233108

[28] Klar P, Lidorikis E, Eckmann A, Verzhbitskiy I A, Ferrari A C and Casiraghi C 2013 Raman scattering efficiency of graphene *Phys. Rev.* B **87** 205435